Chemical Engineering Journal 521 (2025) 166903

Contents lists available at ScienceDirect

Chemical Engineering Journal

journal homepage: www.elsevier.com/locate/cej

Modelling the feasibility of membrane integration into periodic open cellular structures for ammonia decomposition

S. Richard [a,d], D. Tasso [a], M. Rajana [a], A. Saker [a], N. Meynet [a], B. Hary [b], S. Nardone [b], G. Marino [c], C. Italiano [c], A. Vita [c], F. Gallucci [d,*]

[a] ENGIE Lab CRIGEN, 4 Rue Joséphine Baker, Stains, France
[b] ENGIE Laborelec, Rodestraat 125, 1630 Linkebeek, Belgium
[c] CNR-ITAE, Via Salita S. Lucia sopra Contesse n.5, S. Lucia, 98126 Messina, Italy
[d] Sustainable Process Engineering, Chemical Engineering and Chemistry, Eindhoven University of Technology, Den Dolech 2, 5612 AZ Eindhoven, the Netherlands

ARTICLE INFO

Keywords:
Membrane reactor
POCS
Concentration polarization
Additive manufacturing
Ammonia
Hydrogen
Permeation

ABSTRACT

Ammonia is one of the leading carriers for the storage and transport of renewable hydrogen, but its deployment requires compact and scalable technologies for efficient decomposition and purification. This study investigates how operating conditions and design factors impact external mass transfer in Porous Open Cellular Structures (POCS) interfaced with Pd-based membranes. To achieve this, a dip/spin coating method was optimized to deposit Ru based catalytic layer onto nickel alloy POCS produced via Selective Laser Melting (SLM), and kinetic activity was tested providing validation basis for CFD modelling activities. Numerical permeation tests highlighted the influence of packing type and porosity, revealing that the Kelvin 3-0.6 with baffles performed best at a Gas Hourly Space Velocity (GHSV) below 1211 h^{-1}, achieving higher hydrogen recovery and minimized concentration polarization. At higher GHSV, baffles improved the Concentration Polarization Coefficient (CPC) but resulted in slightly lower hydrogen recovery compared to baffle-free configurations. The study of ammonia decomposition in a Kelvin cell POCS membrane reactor revealed that optimizing POCS membrane reactors requires balancing hydrogen production kinetics with the extraction driving force. Hydrogen production increased with GHSV, peaking at 1850 h^{-1} before declining due to non-permeating gas accumulation, and a similar trade-off was observed with porosity, where optimal performance occurred at 0.8 porosity before kinetic limitations caused hydrogen recovery to decline. Overall, optimizing POCS membrane reactors involves a balance of hydrogen production and extraction, and the integration of baffles has the potential further boost performance. Certainly, POCS could yield economic benefits by protecting the membrane and reducing mass transfer limitations, requiring less membrane area for a given separation.

Nomenclature

BCC	Body-Centered Cubic cell
CAD	Computer-Aided Design
CFD	Computational Fluid Dynamic
CP	Concentration Polarization
CPC	Concentration Polarization Coefficient
DNS	Direct Numerical Simulation
FDM	Fused Deposition Modelling
GHSV	Gas Hourly Space Velocity
HRF	Hydrogen Recovery Factor
KC	Kelvin Cell
LPBF	Laser Powder Bed Fusion
MAPE	Mean Absolute Percentage Error
MR	Membrane Reactor
OCF	Open-Cell Foam
POCS	Periodic Open Cellular Structure
PBR	Packed Bed Reactor
PBMR	Packed Bed Membrane Reactor
RANS	Reynolds-Averaged Navier-Stokes
SCS	Solution Combustion Synthesis
SLM	Selective Laser Melting
SEM	Scanning Electron Microscopy
SSA	Specific Surface Area
TPMS	Triply Periodic Minimal Surface
TGA	Thermogravimetric Analysis
WSV	Weight Space Velocity

(continued on next column)

(continued)

* Corresponding author.
E-mail address: F.Gallucci@tue.nl (F. Gallucci).

https://doi.org/10.1016/j.cej.2025.166903
Received 8 March 2025; Received in revised form 2 August 2025; Accepted 5 August 2025
Available online 7 August 2025

Symbols

d_c	Cell length	m
d_s	Strut diameter	m
P_{in}	Inlet pressure	bar
P_{ret}	Retentate pressure	bar
P_{perm}	Permeate Pressure	bar
Pe	Permeability	$mol \cdot m^{-2} \cdot s \cdot bar$
E_{act}	Activation Energy	$J\ mol^{-1}$
S_{POCS}	Total POCS surface (in contact with fluid)	m^2
s_{cat}	Thickness of the coating layer	m
T	Fluid temperature	°C
v	Fluid velocity	$m \cdot s^{-1}$
μ	Dynamic viscosity	Pa·s
ϵ	Porosity	–
ρ	Fluid density	$kg \cdot m^{-3}$

1. Introduction

With an ever-increasing penetration of renewable energy, the role of green hydrogen, produced through electrolysis, is increasingly acknowledged but faces challenges in transport and storage, due to its need for extreme cooling to −253 °C [1]. Ammonia, a carbon-free alternative, can be efficiently liquefied at 10 bar or −33 °C, providing a denser energy storage option with 13.77 MJ/L, compared to 8.5 MJ/L for liquid hydrogen and 4.5 MJ/L for compressed hydrogen [2–4]. According to the International Energy Agency (IEA), ammonia could surpass hydrogen in economic viability for distances exceeding 3500 km, making it a superior choice for long-range distribution of renewable energy [5]. Additionally, ammonia benefits from a mature infrastructure, robust regulations, and a strong safety record, with most major ammonia-related accidents involving derivatives like ammonium nitrate rather than ammonia itself [6,7]. Overall, ammonia stands out as an efficient, cost-effective, CO_2-free energy storage option. The catalytic decomposition of ammonia into high-purity hydrogen, which had been commercially underutilized, is now gaining attention as a key method for utilizing ammonia as a hydrogen carrier. This process is particularly relevant for applications such as fuelling stations and both onboard and stationary Proton Exchange Membrane (PEM) fuel cell generators [8]. The conventional process typically requires a high-temperature reactor (above 700 °C) using a nickel-based catalyst in a Packed Bed Reactor (PBR). However, precious metals like rhodium, iridium, platinum, and especially ruthenium, all part of the Platinum Metals Group (PMG), have shown to enhance catalytic activity significantly [9–12]. This process produces a gas mixture from which hydrogen is commonly separated using Pressure Swing Adsorption (PSA), though alternatives like cryogenic separation or ion-exchange zeolites are also employed [13]. To address the challenges of reaction temperature and downstream gas separation, researchers are turning to membrane reactors (MR). This technology directly extracts hydrogen from the catalytic bed, bypassing equilibrium constraints and improving reaction kinetics [14]. As a result, it reduces, or even eliminates, the need for downstream purification, leading to increased compactness and overall system efficiency. Palladium-based membranes are often favored for such applications due to their excellent hydrogen permeability, selectivity, and thermal stability [13]. One of the earliest investigations into ammonia decomposition using a self-supported Pd-based membrane reactor was conducted by Collins and Way in the 1990s [15]. Since then, membrane reactor designs have evolved to improve performance and overcome challenges in durability, scalability, and integration [14,16–20]. Developments include double-skin membranes to protect the palladium layer [16], hollow fiber membranes to boost hydrogen recovery through higher surface-area-to-volume ratios [19,21], and catalytic membranes that minimize transport limitations by integrating the catalyst directly on the membrane surface [20]. These systems have consistently produced high-purity hydrogen under laboratory conditions, with conversion enhancements of up to 50 % for ammonia decomposition [13,22]. Nevertheless, comparing results across studies remains difficult due to the complex interplay between membrane properties, catalyst formulation, and operating conditions. Even under similar pressure and temperature conditions, variations in specific membrane area, space velocity, and hydrogen partial pressure can lead to significantly different performance outcomes [22]. In most of these studies, the membrane reactor consists of a tubular vessel with vertically inserted membranes surrounded by a packed bed of catalyst. Reactants are typically introduced at the bottom and flow upward through the bed, with hydrogen collected inside the membrane as permeate, while the remaining gases exit as retentate (cf. Fig. 1).

Although simple in design, this packed bed configuration faces challenges like flow channelling, pressure drops, and heat and mass transfer limitations, particularly at larger scales. The low thermal conductivity of packed catalyst beds can create significant temperature gradients, leading to catalyst deterioration and reduced membrane flux and stability. High-flux palladium membranes are also affected by "concentration polarization," caused by the accumulation of non-H_2 species in the retentate, further limiting performance. These challenges can be mitigated by increasing convective forces or adding baffles to induce gas recirculation, thereby enhancing radial heat and mass transfer [23]. Additionally, researchers have explored alternative catalytic configurations like fluidized bed reactors, which enable isothermal operation and reduce mass transfer limitations, though they come with added complexity and the risk of membrane surface erosion. A promising solution to heat and mass transport limitations in catalytic reactors could also lie in the use of cellular structures as alternative catalyst supports. Novel fixed-bed supports like open-cell foam (OCF) have been introduced, enabling fast transverse heat and mass transport with reasonable pressure drops and low contact time. Periodic Open-Cell Structures (POCS) have emerged as innovative catalytic supports with interconnected cells in various shapes (e.g., cubic, diamond, or octet), forming highly regular three-dimensional structures. These supports combine the advantages of OCF by enhancing both axial and radial gas-solid transfer rates while maintaining a consistent and uniform framework. Additive manufacturing (3D printing) offers a potential avenue for tailoring these POCS as catalytic supports for specific applications, enabling advanced optimization of support design to enhance local transport properties in critical reactor sections (e.g., membrane areas or reactor inlets). Additionally, 3D printing can reduce material waste and improve energy efficiency compared to subtractive manufacturing methods [24]. Techniques such as robocasting [25], selective electron beam melting (SEBM) [26], selective laser melting (SLM) [27–29], direct metal laser sintering (DMLS), and stereolithography [30] have already been employed to create highly reproducible POCS. While predominantly investigated in thermohydraulic studies (e.g. heat transfer [31–34] and pressure drop [33,34]), POCS are also beginning to demonstrate promising success in reactive processes affected by external heat and mass transfer limitations. These include methanation [25,35], methanol synthesis [36], Fischer-Tropsch [37], methane reforming [38,39] or methanol reforming [40], ammonia cracking [41] and CO oxidation [30,42] methanol oxidation [29]. The advantageous heat transfer properties of POCS have been leveraged to perform isothermal kinetic measurements at elevated temperatures, particularly under low flow rate conditions, where their superior conductive heat transfer outperforms that of conventional packed beds [29]. This enhanced thermal management enables safer operation in harsher environments, such as higher wall temperatures or increased catalyst loadings, while also mitigating catalyst deactivation by maintaining better temperature control. At higher flow rates, however, packed beds may offer improved convective heat transfer, albeit with the trade-off of higher pressure drops. Furthermore, wall coupling plays a critical role in thermal performance: even limited contact areas (10–20 %) can substantially boost

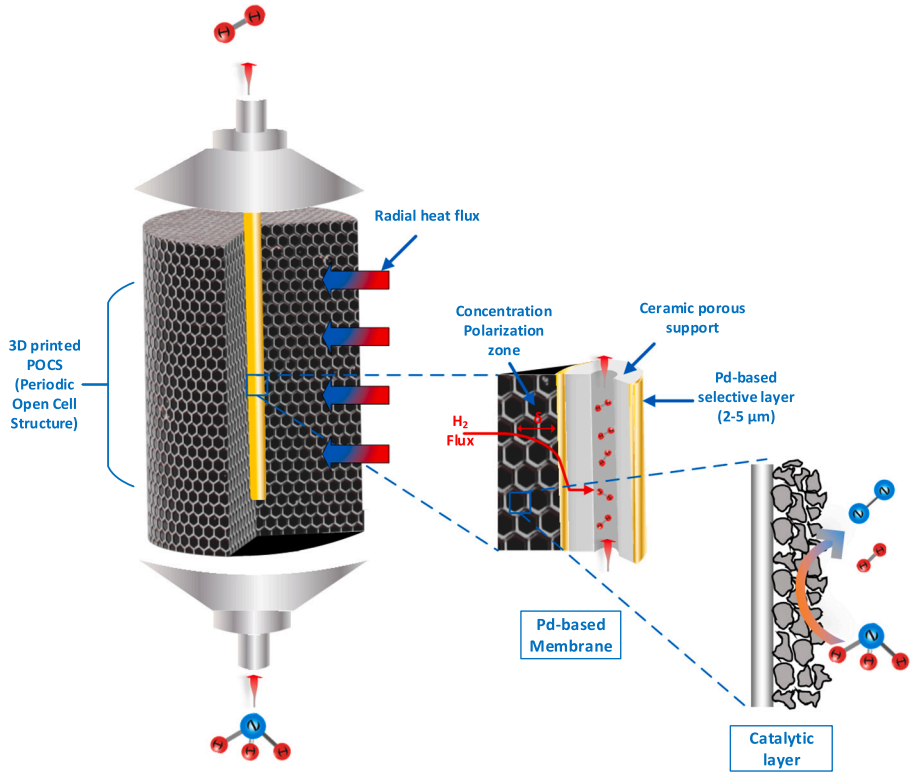

Fig. 1. Illustration of a POCS Membrane Reactor studied for on-site hydrogen production from ammonia cracking. Reactants are introduced from the bottom and move upward, with hydrogen collected inside the membrane as permeate, while other chemical components form the retentate.

heat transfer, as demonstrated by Busse et al. [32]. Compared to pellet beds, especially those with small pellets, POCS typically have lower catalyst holdup due to their open structure, limiting both surface area and catalyst mass per unit volume. For instance, typical packed beds using 1 mm pellets (assuming simple cubic packing with a porosity of ~0.48) can provide specific surface areas exceeding 30 cm^{-1}, whereas 1 cm pellets yield values below 5 cm^{-1}. In contrast, POCS, despite having higher porosities (>0.8), can achieve comparable or even slightly higher specific surface areas ranging from 4 to 14 cm^{-1}, depending on strut thickness, cell size, and geometry [42, p17]. While the fluid–solid interfacial area in POCS may be comparable to or even higher than that of pellet beds, their lower catalyst inventory can be offset by improved catalyst utilization, enhanced heat and mass transfer, and reduced temperature gradients.

Despite the promising benefits of POCS, converting them into active catalytic supports poses significant challenges. With a few exceptions, so-called self-catalytic POCS [40,43], the structures reported so far are typically not catalytically active. The development of uniform catalytic layers over the POCS support, which remain active and stable under the operational conditions of the reactions, is crucial. A variety of activation techniques have been employed [44], involving the deposition of catalytically active phases on metallic supports, including chemical vapor deposition (e.g. Ti–6Al–4V diamond lattice [45]), solution combustion synthesis [38,46], and washcoating (e.g. Iron based OCF [47], Copper-based diamond cell [48] or Aluminium-based cubic cell [42]), each aimed at anchoring a catalytically active phases onto the POCS. Some of these methods involve a series of additional stages after the printing process that can increase the cost of this type of structure. For instance, regardless of the ceramic or metallic nature of the structured support, the washcoating method, commonly used, involves multiple steps: preparing and controlling powder materials, dispersing them in a solvent, adjusting the slurry's viscosity, applying the slurry through dip and spin coating to achieve a homogeneously thick active material layer, followed by drying or calcination, and repeating the process until the desired loading is achieved. Instead, the SCS method seems promising in terms of time reduction. It takes advantage of an exothermic, very quick, and self-sustaining chemical reaction between metal/oxide precursors and an organic fuel (i.e., urea), resulting in the synthesis of nanocrystalline oxide powders directly over the surface of structured supports. However, it is more suitable for the activation of ceramic supports. To effectively design POCS reactors, understanding transport phenomena is crucial.

CFD (Computational Fluid Dynamics) simulation analysis is an effective tool for systematically studying transport phenomena in membrane reactors, addressing issues related to scale-up and the addition of internal components [23,49–51]. For instance, Voncken et al. [49] addressed scalability challenges, highlighting that the interaction of polarization zones in a multi-membrane module becomes more significant at smaller inter-membrane distances under fluidization conditions. Choi et al. [23] demonstrated the potential of incorporating baffles in a membrane reactor for methane reforming to enhance performance. Additionally, Ma et al. [50] explored the variation of radial mass transfer limitations, noting significant membrane tube-to-tube differences in a multi-tube module, particularly severe under low flow rates. Unlike experimental measurements, which require specialized infrastructure for sample preparation and testing, numerical simulations are generally more cost-effective and faster to implement. They also enable detailed analysis prior to reactor construction, allowing for the exploration of multiple configurations to identify the optimal design while providing an understanding of how reactor geometry influences transport phenomena. From the perspective of external mass transfer in Periodic Open-Cell Structures (POCS), several studies have explored this topic using CFD. These studies often compare different POCS cell types [52,53], benchmark them against conventional supports [53], or introduce variations to the basic POCS design to create anisotropy [54,55]. For example, Ferroni et al. [56] compared Kelvin and Diamond cell POCS for mass transfer under similar specific surface areas. They found that Diamond cells performed better at lower velocities (v = 5 m/

s), while both Kelvin and Diamond cells showed similar performance at higher velocities (v = 25 m/s). Their findings also suggest that these POCS structures could outperform state-of-the-art honeycomb substrates in mass transfer at higher flow rates. Additional details regarding whether the comparisons were conducted under equivalent specific surface areas would provide further insight. Kaur et al. [31] observed that among various unit cell geometries, the Octet structure exhibited the highest volumetric Nusselt number, followed by the Kelvin, Cube, and Face-Diagonal Cubic (which includes an additional diagonal strut on each face) structures, particularly at low velocities (0.5–3 m/s) under comparable porosity conditions. In all four topologies, the primary mechanism for heat transfer enhancement at low velocities was stagnation-type flow. Papetti et al. [54] conducted a numerical and experimental study on mass transfer in open-cell lattice structures with different cell shapes. They found that POCS had better transport properties compared to honeycomb monoliths, with Kelvin and tilted cubic cells achieving higher mass transfer rates than simple cubic cells.

Despite the potential of Periodic Open-Cell Structures (POCS) to enhance mass and heat transfer processes, limited information exists regarding their interaction with high-flux Pd-based membranes, necessitating further analysis. This work aims to provide initial insights into how operational conditions and design parameters influence external mass transfer in POCS interfaced with hydrogen-selective Pd-based membranes during hydrogen separation and ammonia decomposition in a membrane reactor, as illustrated in Fig. 1. To achieve this, a dip/spin coating method was optimized to deposit Ru-based catalytic layers onto IN625 POCS produced via Selective Laser Melting (SLM), and kinetic activity was tested to provide a validation basis for the subsequent modelling activities. Computational Fluid Dynamics (CFD) simulations, validated against the experimental results, were employed to extend the analysis to POCS interfaced with a palladium membrane. The model was used to investigate the impact of POCS design parameters (e.g., porosity, cell type) and flow conditions on external mass transfer. The findings of this study could influence future designs of POCS membrane reactors.

2. Experimental set up

2.1. Manufacturing of the structures

As described in our previous publication [53], nickel alloy POCS samples with various cell types (e.g., body-centered cubic, Kelvin, and gyroid) were fabricated using an SLM280 Laser Powder Bed Fusion (LPBF) machine at ENGIE Laborelec, based on CAD designs. The cylindrical samples measured 10 mm in diameter and 15 mm in height. Overall, the printed samples closely matched their CAD models, with porosity deviating by no more than 15 % from the intended design. Table 1 summarizes the design parameters, including materials, strut diameter, cell length, porosity, and specific surface area relevant to this work. The notation used for the POCS samples begins with the cell type geometry, followed by numbers representing the cell and strut sizes in millimeters, respectively.

Table 1
Geometrical features of the CAD design cell parameters printed relevant to this study. The POCS structures are denominated by the cell type followed by the size of the cell and the strut size.

Cell type	Cell length, d_c [mm]	Strut diameter, d_s [mm]	Theoretical porosity, ϵ %	Theoretical specific surface area, SSA [cm^{-1}]
BCC 3-0.4	3	0.4	0.91	8.1
BCC 3-0.75	3	0.75	0.73	12.3
Kelvin 3-0.6	3	0.6	0.79	12.16
Kelvin 3-0.61	3	0.61	0.79	12.3

Table 1 summarizes the design parameters, including materials, strut diameter, cell length, porosity, and specific surface area relevant to this work. The notation used for the POCS samples begins with the cell type geometry, followed by numbers representing the cell and strut sizes in millimeters, respectively.

2.2. Catalyst synthesis and POCS activation

The catalytic activation of the nickel alloy POCS samples by CNR-ITAE follows a multi-step process. It involves catalyst powder preparation, ball milling, optimizing slurry preparation, and applying the slurry to the pretreated metallic structure using a dip-and-spin coating method. Following Doh et al. [57], the solid oxide catalyst powder, $Sr_{0.84}Y_{0.16}Ti_{0.92}Ru_{0.08}O_{3-\delta}$, is synthesized via a modified Pechini method, a sol-gel technique producing fine, highly dispersed catalyst powders with abundant active sites [58]. This method involves dissolving metal salts in a solution, adding citric acid as a chelating agent to form a metal complex, and reacting it with ethylene glycol to form a solid resin. This solid is then ground and sieved through a 250 μm-diameter sieve to ensure uniform composition and size. After drying and calcining, the resin transforms into a homogeneous metal oxide powder with a Ru content of 4 wt%. References for the product used, along with detailed preparation steps, can be found in Appendices C and D. The powder's physicochemical properties were analyzed using nitrogen physisorption, X-ray diffraction and temperature-programmed reduction, with the results provided in Appendix F.

The slurry preparation was optimized using a dispersion medium of hydrolyzed polyvinyl alcohol (PVA) and bi-distilled glycerol in distilled water, incorporating ball-milled catalyst and boehmite alumina powders (Disperal P2®, Sasol) for enhanced dispersion. Disperal P2® in water is also used to improve the adhesion of the washcoat. The slurry's rheology, critical for achieving a stable and uniform coating, is characterized with a rotational rheometer (Modular Compact Rheometer MCR 92, Anton Paar GmbH, Graz, Austria). A shear thinning behaviors was found with a viscosity value between 0.08 and 0.07 Pa·s in the typical shear range for the spin-coating applications (1000–2000 s^{-1}), in this range the slurry assume a Newtonian behaviour (see Fig. 2.B). The optimized slurry is then applied to a pretreated metallic structure (Kelvin 3-0.6), calcined at 900 °C, using a combined dip and spin coating process. This process involves immersing the structure for 10 s, followed by removal of excess liquid with a commercial spin-coater (SPIN 150 SPS Europe), where parameters such as rotation speed and duration are carefully adjusted to achieve the desired material loading. A picture of the spin coater is shown in Fig. 2.C. The coating process involves multiple dips and spins to achieve a catalyst load of 0.16 g/cm^3 (0.19 g), as shown in Fig. 2.D.

Gravimetric analysis is performed after each flash drying step and the final calcination to monitor weight changes and assess the washcoat load. The final washcoat load is determined by the weight difference between the bare and coated POCS. The washcoat thickness (s_{cat}) is estimated from the specific load as per Eq. (1), as precise instrumentation to cut the metallic structure were lacking.

$$mass\ of\ catalyst[kg] = \rho_{cat}\left[\frac{kg}{m^3_{coating}}\right] * \overbrace{SSA\ \left[m^{-1}\right] * V_{reactor}\left[m^3\right] * s_{coating}[m]}^{Volume\ of\ catalyst\ \left[m^3_{coating}\right]}$$

$$\leftrightarrow s_{coating} = \frac{mass\ of\ catalyst[kg]}{\rho_{cat}\left[\frac{kg}{m^3_{coating}}\right] * SSA\ [m^{-1}] * V_{reactor}[m^3]} = \frac{0.19 * 10^{-3}[kg]}{2044\left[\frac{kg}{m^3_{coating}}\right] * 1210\ [m^{-1}] * 1.17 * 10^{-6}[m^3]} = 65\ \mu m \quad (1)$$

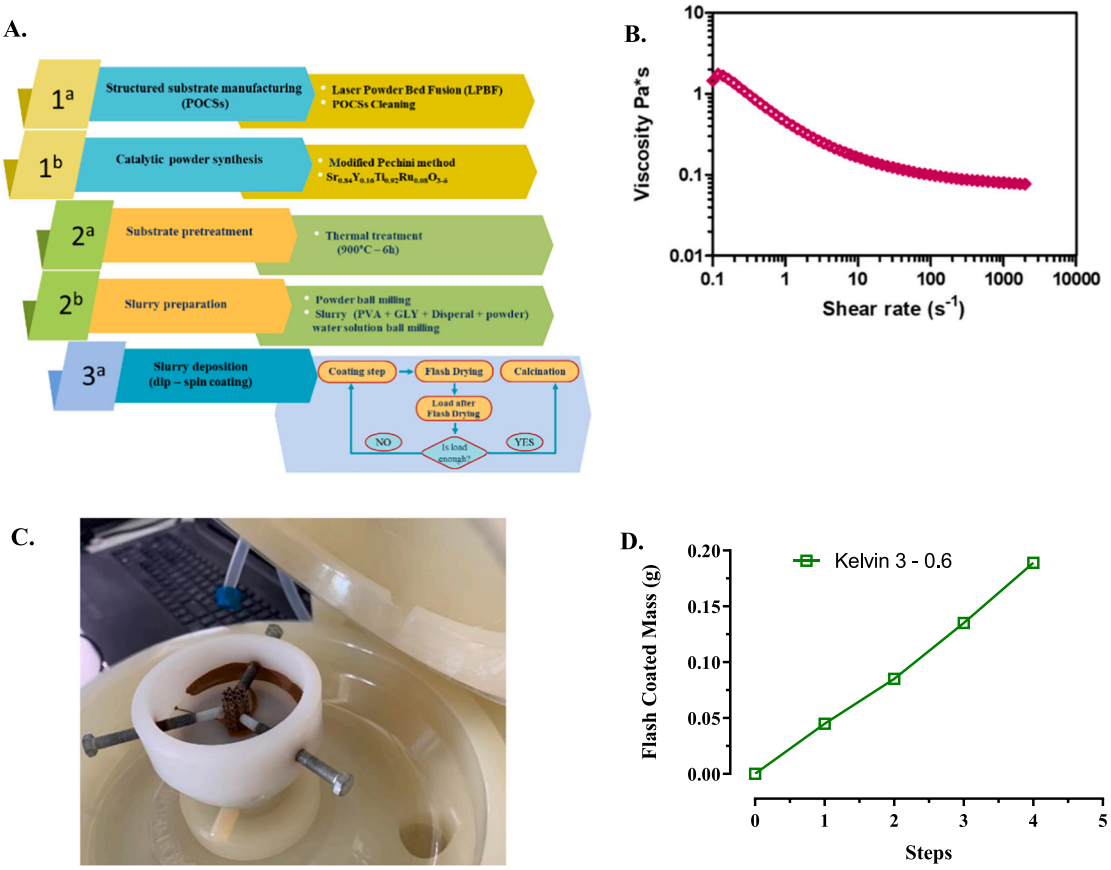

Fig. 2. A. Summary of main steps involved in the preparation of the coated POCS B. Rheological behaviour of the slurry C. Photo of the spin coating step D. Loading curve.

where the coated volume (*Vcoat*) corresponds to the whole sample in the case of foam replicas. The main physico-chemical features of the synthesized powders are reported in Table 2. As a first approximation, the catalytic loading C_{load} was calculated from these tests, defined as the mass of catalyst deposited per unit surface area of the POCS. In the subsequent numerical investigation, this parameter will serve as a factor in converting volumetric reaction rates into surface reaction rates.

The adherence of the coating layer was assessed by measuring the weight loss after ultrasonic treatment in a petroleum ether bath for 30 min. The coated POCSs underwent ultrasonic treatment at 45 kHz and 130 W using the USC 900D ultrasonic bath, followed by drying at 120 °C for 1 h. The mechanical stability was reflected by a weight loss of 1.2 % relative to the loaded layer.

A Keyence VHX-7000 digital optical microscope characterized by a fully integrated head that use a stage shift technology and 4 K mode for high resolution imaging was also used for morphological measurements. Detailed images of the POCS were taken with VHX-E20 (High-Resolution, Low Magnification Objective Lens 20–100×) and VHX-E100 lenses (High-Resolution, Medium Magnification Objective Lens 100–500×).

Table 2
Geometrical characteristic of the Kelvin 3-0.6 POCS (*Assumed **Calculated ***Measured).

Catalyst composition (wt%)	Ru (4.3 %), Ti (23.43 %), Y (7.57 %), Sr (39.16 %), O (25.54 %)
$\rho_{dense}\left(\frac{kg_{cat}}{m^3_{cat}}\right)$ **	2921
$\epsilon_{coating}\left(\frac{m^3_{void}}{m^3_{coating}}\right)$ *	0.3
$\rho_{cat}\left(\frac{kg_{cat}}{m^3_{coating}}\right)$ **	2044
$\rho_{bed}\left(\frac{kg_{cat}}{m^3_{bed}}\right)$ **	429
*Mass of catalyst (g)***	0.19
Thickness of the coating, s_{cat} (μm) calculated from Eq. (1) **	65
Loading $\left(\frac{mg}{cm^2_{POCS}}\right)$ **	13.2
Loading, C_{load} $\left(\frac{mg}{cm^3_{reactor}}\right)$ **	0.16

2.3. Kinetic tests

Tests of the catalytic activity of the ammonia decomposition reaction were conducted by flowing a stream of 50.1 % ammonia to a fixed reactor, at WSV of 95 mL·min^{-1} (WSV 30000 cm^3·g$_{cat}^{-1}$·h^{-1}). The catalyst was reduced at a temperature of 600 °C for 1 h. The ammonia conversion and the hydrogen formation rate values in the reaction at temperature range of 400–600 °C and 1 atm total pressure. The effluent gases were taken at regular intervals and were analyzed by a Gas Chromatography (Agilent 7890A) equipped of three parallel columns (Hayesept Q, HP PLOT Q and Molesive 45/60) connected to a thermal conductivity detector (TCD) using argon as carrier gas.

3. Numerical investigation

3.1. CFD modelling

To examine the effects of morphological features and flow conditions on external mass transport rates in Periodic Open Cellular Structures (POCS) interfaced with palladium selective membranes, CFD simulations were conducted using Comsol™ (version 6.0) for permeation tests

and Ansys Fluent™ (version 2023 R1) for reactor simulations. Three geometrical domains were modelled, as shown in Fig. 3, each with specific dimensions and boundary conditions. The first domain (Fig. 3. A) focused on numerical permeation tests, isolating permeation effects from chemical reactions. The second domain (Fig. 3.B) simulated the experimental setup for validating chemical reactions, while the third (Fig. 3.C) represented a segment of a membrane reactor including both reaction and permeation. In the first domain, isothermal conditions were applied to simplify the analysis of permeation without the influence of temperature variations. In contrast, the second and third domains utilized fully coupled equations for momentum, mass transfer, and conjugate heat transfer, all modelled under laminar flow conditions.

For the "permeation" domain, an active length of 21 mm and a spacing of 0.5 mm were implemented to prevent scratching the sensitive palladium layer, resulting in a total active membrane area of 63 mm^2. Hydrogen permeation through the palladium-silver (Pd—Ag) plated ceramic membrane was simulated under the assumption of infinite selectivity for hydrogen. The hydrogen flux across was modelled using the Richardson equation, as detailed in Eq. (2), ignoring the ceramic support's impact. Additionally, mass transfer limitations on the permeate side are considered negligible, since only virtually pure H_2 is present in that region.

$$J_{H_2} = \frac{Pe}{\delta}\left(p^{n}_{H_{2,ret}} - p^{n}_{H_{2,perm}}\right)\left[\frac{mol}{s\,m^2}\right] \tag{2}$$

where Pe represents the permeability of the membrane, δ denotes the thickness of the selective layer membrane, $p_{H_{2,ret}}$ and $p_{H_{2,perm}}$ represent the hydrogen partial pressure on the retentate and permeate sides, respectively, and n represents the exponential factor that indicates the rate-limiting step of the mechanism by which hydrogen crosses the selective palladium layer. Under ideal conditions, where thermodynamic equilibrium exists between the hydrogen atoms dissolved at the membrane surface and the hydrogen concentration in the gas phase, the pressure exponent n equals 0.5. In this scenario, Richardson equation (Eq. (2)) takes the form of Sieverts' law ($n = 0.5$), suggesting that the diffusion of hydrogen atoms through the bulk of palladium (Pd) is the limiting step in the hydrogen permeation mechanism. The membrane permeability Pe can be expressed using an Arrhenius-type correlation, as described in Eq. (3).

$$Pe = Pe_{0,H_2} e^{-\frac{E_a}{RT}} \tag{3}$$

where Pe_{0,H_2} represents the pre-exponential factor, E_a is the activation energy, R denotes the universal gas constant, and T represents the temperature. The permeation parameters were sourced from Fernandez et al. [59], closely aligned with other similar membrane studies [60].

For the "validation" domain, the geometry consisted of a cylindrical POCS structure, 15 mm in length and 10 mm in diameter. A free-flow domain of 170 mm upstream was added to prevent inlet diffusion phenomena, accompanied by a 10 mm downstream extension. Inlet velocities varied from 0.01 m/s to 1 m/s, and temperatures ranged from 400 °C to 600 °C, while the outlet pressure was maintained at atmospheric conditions. The cylinder's exterior was subjected to a no-slip boundary condition, and its temperature was set to match the inlet temperature. The surface temperature of the POCS was determined by heat fluxes and material properties, utilizing the characteristics of Inconel in a conjugate heat transfer approach. A 50 % ammonia flow was applied to replicate experimental conditions. The catalyst model employs a zero-dimensional approach, treating the reacting layer as infinitesimally thin and neglecting potential irregularities such as cracks and cavities in the washcoat. In this model, the porous surface functions as both a source of products and a sink for reactants.

For the "membrane reactor" domain, a realistic portion of a membrane reactor was employed, featuring a POCS cylinder that is 27 mm long and 26.6 mm in external diameter, enclosing a central membrane with a diameter of 14 mm. Similar to previous models, a free-flow domain of 170 mm was added upstream of the POCS. Additionally, a 0.2 mm gap was introduced between the POCS and the membrane to prevent damage to the membrane during its insertion into the POCS for real-world applications. In practice, an even larger gap might be necessary to accommodate further imperfections in the POCS or facilitate the reactor assembly process, ensuring the membrane remains undamaged. To optimize computational resources, only one-eighth of the domain was modelled, with symmetry boundary conditions applied to two selectively chosen cutting planes. Indeed, Kelvin and BCC structures are inherently symmetric onto these planes (as shown on Fig. 3.C), and the whole domain can be defined by the symmetrical replication of this eight of the structure. Pure ammonia (NH_3) was introduced at the bottom inlet of the reactor, with a no-slip boundary condition applied to the surrounding walls of the reactor bed and both ends of the membrane. The hydrogen generated within the reactor and permeating through the membrane was simulated using the Richardson equation for hydrogen flux, as detailed in Eq. (2).

From the numeric viewpoint, the chosen meshes comprise approximately 400,000 cells for the permeation domain approximately 1 million cells for "validation" domain, and around 8 million for membrane reactor simulations, encompassing both the fluid and solid domains. CFD calculations are performed to model pure laminar flow regime through a POCS structure on which an ammonia cracking reaction is taking place. Gradient computations were handled using the Least Square Cell-Based discretization scheme, while the Second Order Upwind scheme was adopted for the discretization of transport properties,

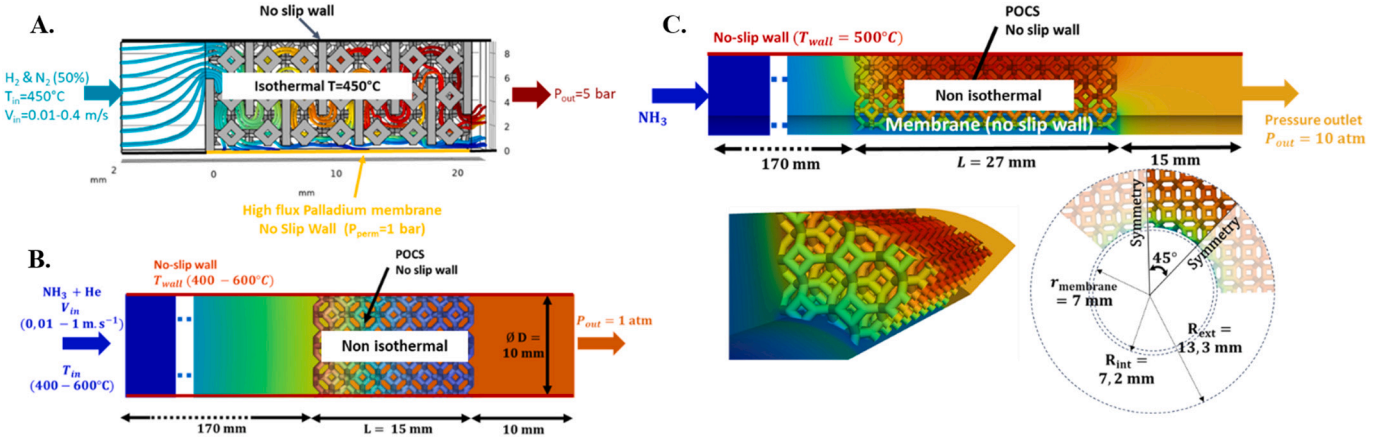

Fig. 3. Implemented boundary conditions and physical setups A. Permeation domain setup B. Traditional reactor mirroring the experimental one, used to validate the chemistry C. Membrane reactor.

including momentum, energy, and turbulence variables. The "coupled" algorithm was chosen for pressure-velocity coupling, ensuring a stable and rapid convergence in this steady-state analysis. Convergence was deemed achieved when the residuals fell below 10^{-4}. A more comprehensive overview of the computational methods, encompassing domain, grid generation, is presented in Appendices G and H.

3.2. Kinetic rate law

A mathematical expression for the intrinsic rate of ammonia decomposition is essential for numerical simulations. These equations link the reaction rate to the reactants' concentrations or partial pressures. However, a widely accepted reaction rate expression for ammonia decomposition is yet to be established. The stoichiometric decomposition of ammonia into H_2 and N_2, as shown in Eq. (4), is mildly endothermic and thermodynamically favored at high temperatures. According to Le Châtelier's principle, the reaction is also favored at low pressure due to molar expansion during decomposition.

$$NH_3 \leftrightarrow \frac{1}{2}N_2 + \frac{3}{3}H_2 \Delta H_f^{\circ} = 45.9\frac{kJ}{mol} \tag{4}$$

Several studies have used Temkin-Pyzhev-like power laws, as described in Eq. (4) to match the experimental conversion [61,62]. This model, while straightforward, has been found to predict empirical data by fitting the reaction order β, activation energy E_{act}, and the pre-exponential factor k_0. Their values are given in the results section in Table 3.

$$R_{NH_3} = k_0 e^{-E_0/RT}\left(\frac{p_{NH_3}{}^2}{p_{H_2}{}^3}\right)^{\beta} \tag{5}$$

The kinetic parameters were determined through a nonlinear least squares method using a Nelder-Mead solver based on the simplex algorithm. This was conducted alongside solving a simple plug flow mass balance for a tubular reactor. Although Nelder-Mead does not guarantee convergence to the optimal solution, several successive optimizations starting from the obtained solution point were performed to yield a better estimation. The fitting was assessed using the Mean Absolute Percentage Error (MAPE) offering a percentage-based evaluation of prediction errors as per Eq. (6).

$$MAPE = \frac{100}{N}\sum_{i=1}^{N}\left|\frac{X_{exp,i} - X_{fit,i}}{X_{exp,i}}\right| \tag{6}$$

where $X_{exp,i}$and $X_{fit,i}$ represent the ammonia conversions obtained from experimental measurements and the model, respectively. To convert this expression to a surface rate law, as demonstrated in the previous chapter, it is multiplied by the catalyst loading C_{load}

$$R_{NH_3} = R_i' * C_{load} = \frac{mol}{kg_{cat}s} * \frac{kg_{cat}}{m^2} = \frac{mol}{m^2 s} \tag{7}$$

3.3. Performance index

Several metrics are used to evaluate the performance of the membrane reactor, including ammonia conversion (X_{NH_3}), defined as the ratio of NH_3 consumption rate to the NH_3 flow rate at the reactor inlet, and the hydrogen recovery factor (HRF), which measures the amount of pure H_2 separated by the membrane relative to the total H_2 produced based on reaction stoichiometry. Both metrics are defined in Eqs. (8) and (9), respectively. However, HRF alone does not provide a comprehensive understanding of potential mass transfer limitations within the reactor, as a low HRF may result from either low membrane permeance or poor gas-phase mass transfer. Therefore, the degree of concentration polarization is evaluated using the Concentration Polarization Coefficient (CPC) [51], as defined in Eq. (10). It represents the ratio of the average H_2 concentration at the membrane surface to that at the wall. The closer the CPC is to 1, the greater the influence of concentration polarization. Additionally, the gas hourly space velocity (GHSV) is calculated as the normal volumetric flow rate of NH_3 relative to the reactor volume.

$$X_{NH_3} = \frac{F_{NH_3,in}^{Ret} - F_{NH_3,out}^{Ret}}{F_{NH_3,in}^{Ret}} \tag{8}$$

$$HRF_{NH_3} = \frac{F_{H_2,out}^{Per}}{\frac{3}{2}F_{NH_3,in}^{Ret}} * 100 \tag{9}$$

$$CPC = 1 - \frac{driving\ force_{real}}{driving\ force_{ideal}} = 1 - \frac{\left(p_{H_2}^{surface-membrane,ext}\right)^{0.5} - \left(p_{H_2}^{permeate}\right)^{0.5}}{\left(p_{H_2}^{surface-wall,ext}\right)^{0.5} - \left(p_{H_2}^{permeate}\right)^{0.5}} \tag{10}$$

$$Recovered\ hydrogen\ flow = \int_{A_p} F_{H_2,out}\, dA_p \tag{11}$$

In those equations $F_{i,in}$ and $F_{i,out}$ are the species molar flowrates at the inlet and outlets of the reactor, respectively. $p_{H_2}^{surface-membrane}$ & $p_{H_2}^{surface-wall.ext}$ designate a surface average of hydrogen partial pressure over the membrane and opposite external wall, respectively.

4. Results

4.1. POCS coating characterization

A photograph of the Kelvin 3-0.6 structure before and after coating is shown in Fig. 4, where a uniform washcoat layer is visible. The structures generally retained their original morphology, featuring hexagonal and square windows, with the smaller square windows being more prone to clogging. After applying the catalytic coating, the structures displayed a brownish hue. Visual inspection revealed that additional material tends to accumulate at the strut intersections or nodes, particularly at the nodes of cubic windows. This accumulation is consistent with reports in the literature for cubic cells and is also observed in honeycomb structures at the edges of the channels [29].

4.2. Kinetic tests & model validation

The catalytic performance of the structured catalyst Kelvin 3-0.6 in ammonia decomposition was evaluated over a temperature range of 400–600 °C. Ammonia conversion increased with temperature, peaking between 500 °C and 600 °C, which is consistent with the endothermic nature of the reaction and its approach to equilibrium, as shown in Fig. 5. The kinetic law parameters derived from Eq. (5) were fitted and are shown in Table 3. The experimental and simulated results showed good agreement, with deviations within ±10 %. This model is now capable of providing valuable insights into how morphological features and flow conditions influence external mass transport rates in POCS, both with and without selective membranes.

Table 3
Kinetic parameters of Eq. (5).

$k_0\left[\frac{mol}{m_{bed}^3\ s\ bar^{-\beta}}\right]$	1.39e15
$E_0\left[\frac{kJ}{kmol}\right]$	2.15e5
$\beta[-]$	0.370

4.3. Permeation tests

Numerical permeation tests were conducted at T = 500 °C, P_{ret} = 5

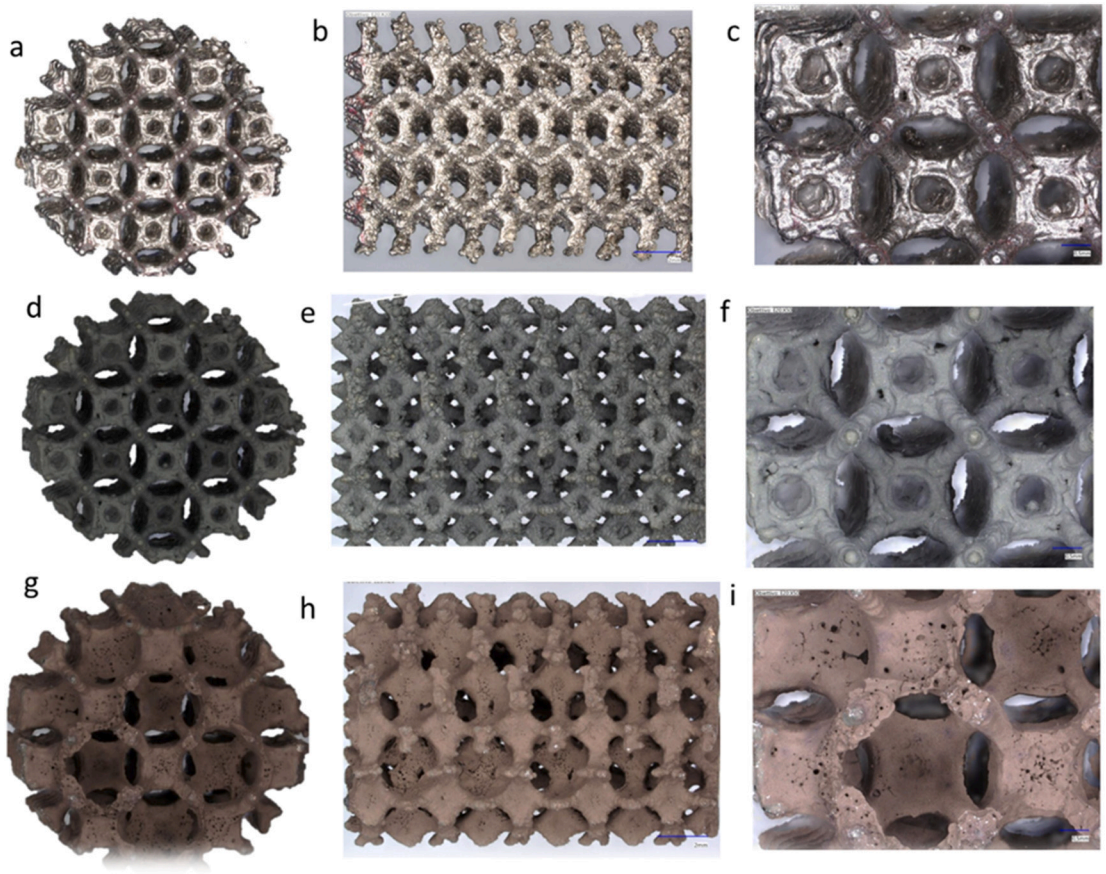

Fig. 4. Optical microscopic images of a–c) Fresh kelvin d–f) After 900 °C 6 h, g–i) after washcoating.

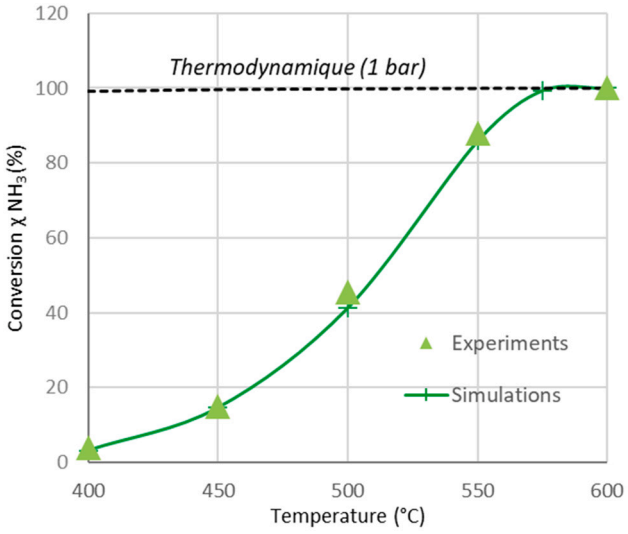

Fig. 5. Fitting of reaction rate model based on Kelvin 3-0.6. The points are the experimental data, the line corresponds to the numeric results.

bar, and P_{perm} = 0.1 bar to evaluate the effects of configuration type (Kelvin cell, Kelvin cell with baffles, BCC, empty bed, and pellet), porosity, and superficial velocity on permeation, measured by hydrogen recovery factor and the coefficient of concentration polarization (CPC). As shown in Fig. 6, hydrogen depletion near the membrane is significant at low superficial velocities but diminishes at higher flow rates. However, increased flow rates reduce hydrogen recovery due to shorter diffusion times and limited membrane contact. The extent of hydrogen depletion also varies with packing type. Fig. 7.A highlights the impact of configuration type, revealing that the Kelvin 3-0.6 configuration with baffles achieves the best performance at gas hourly space velocity (GHSV) values below 1211 h^{-1}. This configuration maximizes hydrogen recovery while minimizing CPC. At low superficial velocities, the performance ranking is as follows: Kelvin 3-0.6 with baffles > Kelvin 3-0.6 (without baffles) > empty bed > pellet bed. However, at higher GHSV values (GHSV >1211 h^{-1}), the baffles, while still reducing CPC, slightly decrease hydrogen recovery compared to the configuration without baffles. This is likely due to the need to slow down fluid flow for longer membrane contact time at higher velocities. Fig. 7.B examines the influence of porosity on Kelvin cell performance, showing that above GHSV 605 h^{-1}, lower porosity provides the best balance between CPC and hydrogen recovery. Conversely, at GHSV values below 605 h^{-1}, higher porosity performs better by accelerating fluid flow and reducing stagnation. At higher flow rates, lower porosity slows the fluid, increasing membrane contact time and promoting crossflow. Lastly, Fig. 7.C compares the Kelvin 3-0.6 configuration with BCC cells, showing that the Kelvin cell appears to perform better when compared at either the same porosity or specific surface area. This superior performance likely stems from its geometric design, which enhances mass transfer and hydrogen recovery. In contrast, the BCC cell maintains consistent behaviour across varying conditions, possibly due to its more linear streamline pattern, as highlighted in previous studies [53].

4.4. Influence of GHSV on MR performance

Under reaction conditions, using the Kelvin 3-0.6 as a reference (T_{in} = 500 °C, P_{ret} = 10 bar, P_{perm} = 0.1 bar), Fig. 8 illustrates the impact of GHSV on hydrogen production and key performance indicators: NH_3

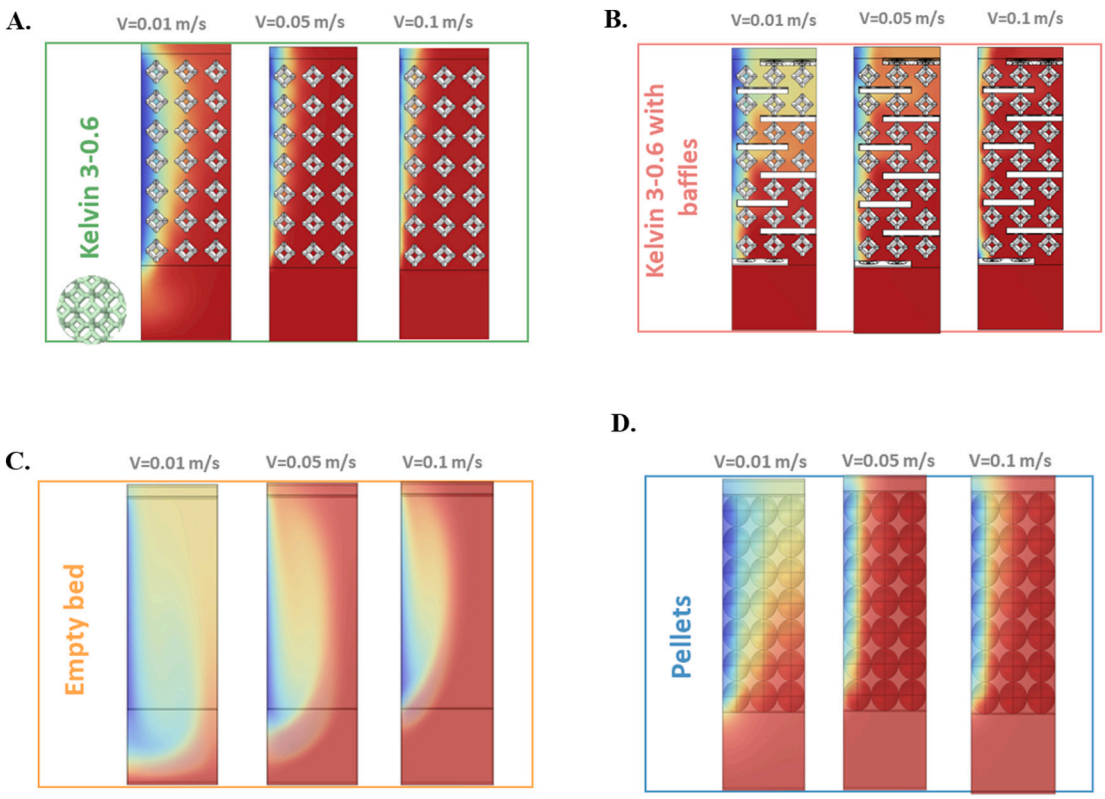

Fig. 6. Numerical simulation results showing the qualitative visualization of the hydrogen molar fraction in baffled A. Kelvin 3-0.6 B. Kelvin 3-0.6 with baffles C. Empty bed D. Pellets (3 mm diameter) (blue = zone depleted of hydrogen).

conversion, HRF and CPC. As shown in Fig. 8.A HRF, conversion, and CPC sharply decline as GHSV increases up to 1850 h^{-1}. Beyond this point, the decreases in HRF and conversion slow, while CPC stabilizes near a plateau. Fig. 8.B shows that although total hydrogen production increases almost linearly with GHSV, the reactor's H_2 productivity (hydrogen permeation through the membrane) peaks at 1850 h^{-1} and then declines. This pattern reflects the dominant effect of concentration polarization at low GHSV (<1850 h^{-1}), where non-permeating gases accumulate near the membrane, reducing hydrogen concentration and extraction rates. At GHSV = 1850 h^{-1}, an optimal balance between hydrogen production and extraction is reached. Above this value, the flow becomes more uniform, which reduces concentration polarization but also lowers conversion, leading to decreased overall hydrogen flux. These observations are consistent with studies by Sitar et al. [20] and Chen et al. [63], which found similar behaviors at different temperatures and GHSVs, as well as Cerrillo et al. [64], who observed peak performance in a similar GHSV range. Fig. 9 presents the contour plots of hydrogen concentration at various GHSV levels, outlining different regimes. Ultimately, the optimal balance between conversion-limited (low recovery) and permeation-limited (high recovery) regimes depends on the overall process flowsheet. When maximizing hydrogen recovery is the priority, productivity may need to be sacrificed by operating near the permeation-limited regime, where the membrane's extraction capacity exceeds the rate of hydrogen generation, potentially resulting in uneconomical operation due to large membrane areas or very low GHSV. Conversely, if the hydrogen-rich retentate is used to supply heat for the endothermic reaction, operating closer to peak productivity with lower H_2 recovery becomes more advantageous. These trade-offs must be evaluated at the process integration level, based on economic and efficiency criteria. Reactor geometry (e.g., specific membrane area) and operating conditions should be carefully tuned to the selected catalyst–membrane combination.

4.5. Impact of porosity on MR performance

Under the reference conditions of GHSV = 4500 h^{-1}, T_{in} = 500 °C, P_{ret} = 10 bar, and P_{perm} = 0.1 bar, Fig. 10.A and B illustrate how POCS porosity impacts hydrogen production and performance metrics. As porosity increases, NH_3 conversion declines due to a reduced specific surface area, resulting in lower total hydrogen production and retentate hydrogen content. Interestingly, both the hydrogen recovery factor and permeate hydrogen initially rise with porosity, reaching a peak around 0.8 before decreasing. This behaviour indicates that at lower porosities, the process is rather limited by permeation (i.e. not enough membrane area). Under those operating conditions, a porosity of approximately 0.8 achieves an optimal balance between hydrogen production and extraction, maximizing recovery. Beyond this point, hydrogen production becomes kinetically constrained by insufficient hydrogen partial pressure, limiting further recovery. Therefore, optimal membrane reactor operation requires balancing the kinetics of hydrogen production from ammonia decomposition with the driving force for hydrogen extraction, tailored to specific operating conditions. These observations are visually substantiated by Fig. 11, which shows the H_2 fraction streamlines for each porosity value investigated, along with the corresponding operational regimes. The streamlines clearly demonstrate how changes in porosity affect hydrogen distribution.

5. Conclusions

This work aimed at offering initial insights into the influence of operational conditions and design parameters on external mass transfer in POCS integrated with hydrogen-selective Pd-based membranes, specifically during standalone hydrogen separation and ammonia decomposition within a membrane reactor. By integrating experimental results, with numerical simulations, we assess how these factors affect catalytic performance and separation performance.

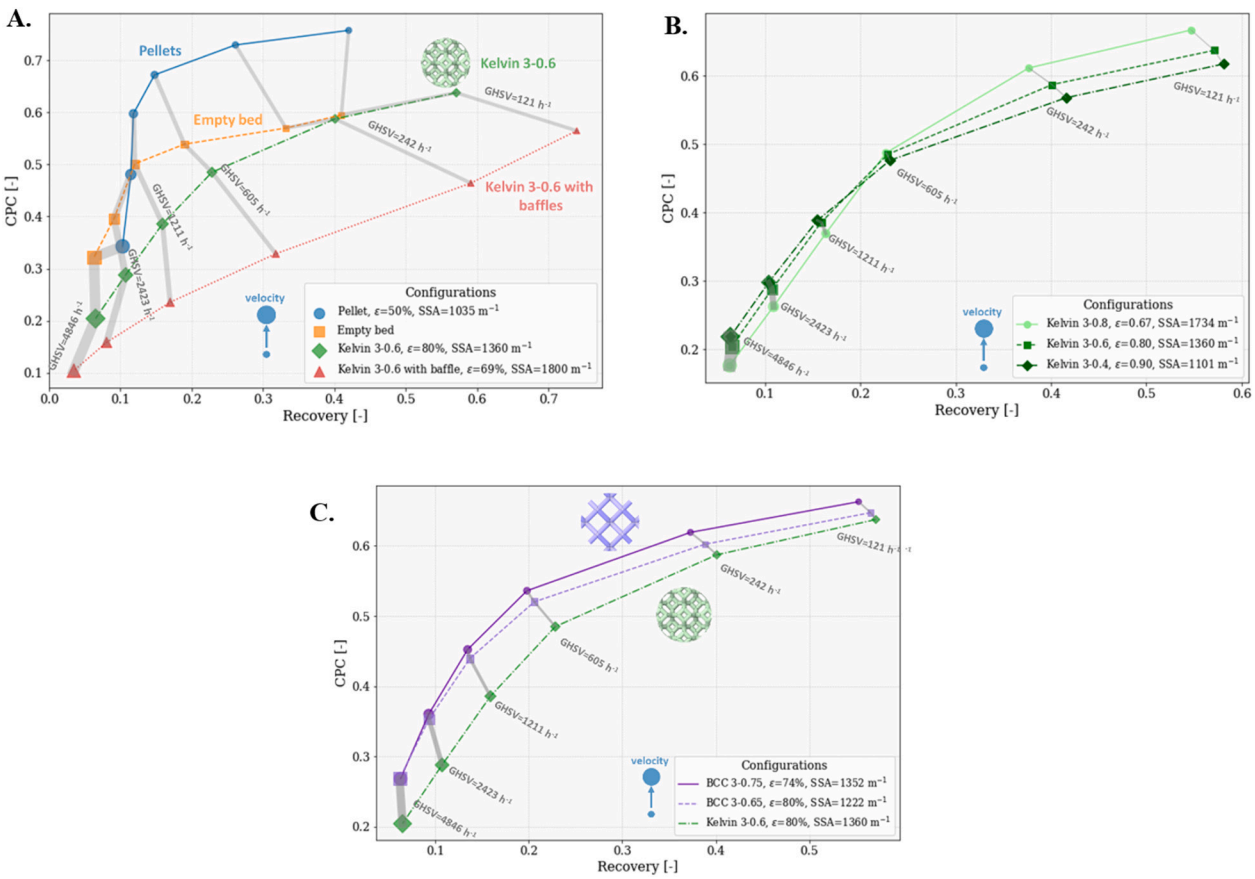

Fig. 7. Numerical simulation results showing the influence of the packing type on the permeation performance under T = 500 °C, P_{ret} = 5 bar, and P_{perm} = 0.1 bar and 50 % H_2 inlet: A. comparison across several configurations comparison of performance between pellets (3 mm diameter), Kelvin 3-0.6, empty bed and B. Impact of porosity on the Kelvin cell type C. Impact of cell type comparison between BCC and Kelvin cells under similar geometric attributes.

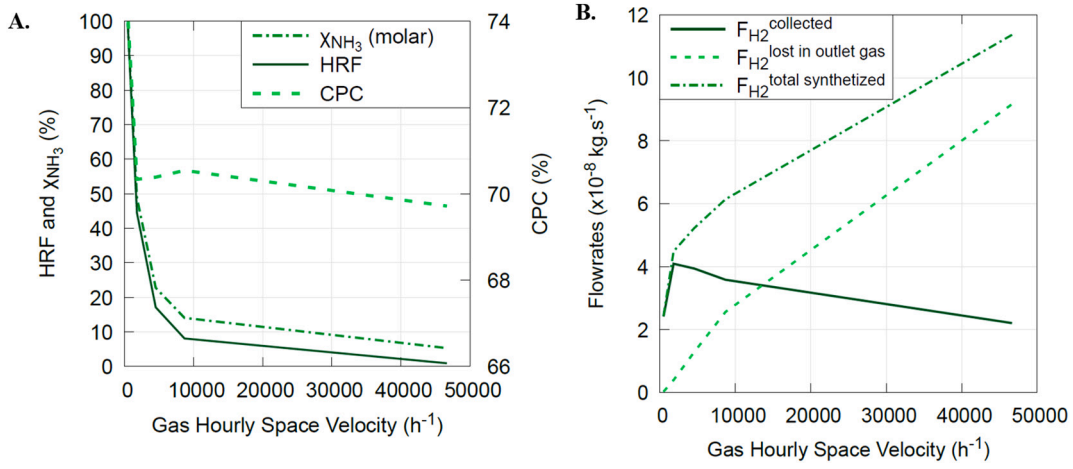

Fig. 8. Numerical simulation results showing the effect of GHSV on the ammonia decomposition using membrane reactor. A. Ammonia conversion, B. hydrogen recovery and recovered H_2 flow rate (T_{in} = 500 °C, P_{ret} = 10 bar, P_{perm} = 0.1 bar).

- A dip/spin coating method was optimized to successfully deposit an Ru-based catalytic layer onto IN625 POCS, produced via Selective Laser Melting.
- Numerical permeation tests evaluated highlighting the effects of packing type and porosity. In particular, the Kelvin 3-0.6 with baffles delivers the best performance below a GHSV of 1211 h^{-1}, achieving higher hydrogen recovery and minimizing the degree of concentration polarization. The performance order Performance order at low superficial velocities: Kelvin 3-0.6 with baffles > Kelvin 3-0.6 (without baffles) > empty bed > pellet bed. At higher GHSV, baffles still show better CPC but slightly lower hydrogen recovery (i.e. hydrogen extraction) compared to the configuration without baffles. In addition, comparing Kelvin and BCC cells, it was shown that the Kelvin cell provides a better permeation performance.
- The impact of GHSV on the membrane reactor equipped with Kelvin cell 3–0.6 was studied: hydrogen production increases with GHSV,

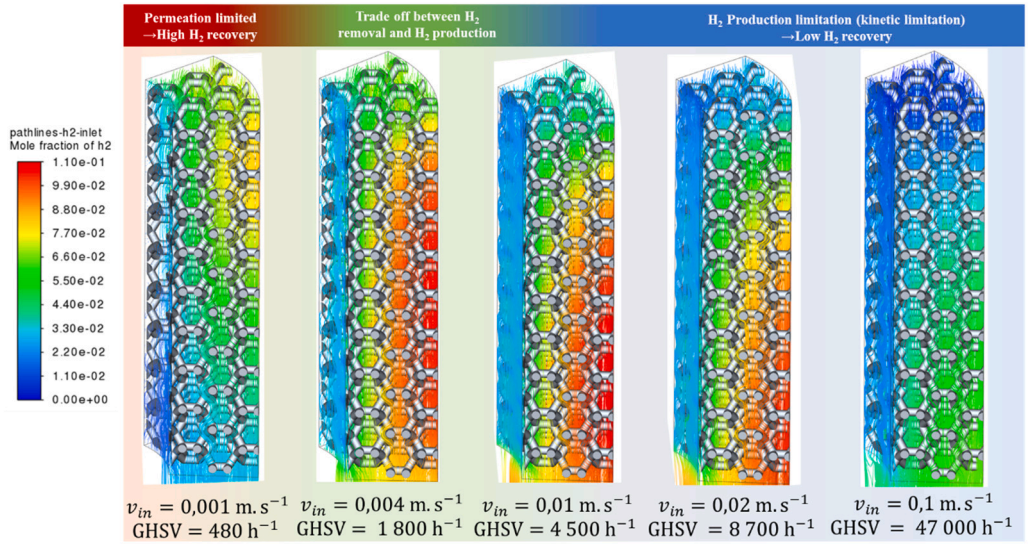

Fig. 9. Contour plot of H_2 mole fraction for different GHSV using Kelvin 3-0.6 on a representative portion of a membrane reactor.

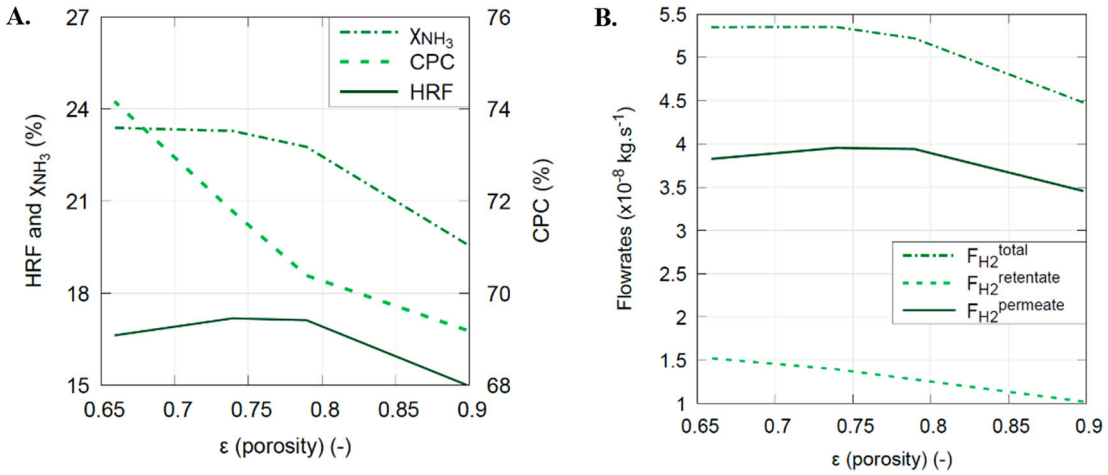

Fig. 10. Numerical simulation results showing A. NH_3 conversion and hydrogen recovery B. Hydrogen productivity for different porosity values of the KC lattice obtained at T_{in} = 500 °C, P_{ret} = 10 bar, P_{perm} = 0.1 bar & GHSV = 4500 h^{-1}.

but reactor productivity peaks at 1850 h^{-1} before declining. At GHSV <1850 h^{-1}, non-permeating gases accumulate near the membrane, reducing hydrogen extraction. At GHSV = 1850 h^{-1}, hydrogen production and extraction are balanced. Beyond this point, increasing GHSV reduces concentration polarization but decreases conversion, leading to lower hydrogen flux.

- A similar trade-off was observed with increasing POCS porosity in the Kelvin cell type, where hydrogen recovery and permeation initially improve, peaking at a porosity of 0.8, but further increases lead to a decline in total hydrogen production due to kinetic limitations, highlighting the importance of balancing hydrogen production and extraction in membrane reactors.

Optimizing the performance of a POCS membrane reactor requires carefully balancing hydrogen production kinetics with the extraction driving force, along with selecting an appropriate POCS structure. POCS not only protect the fragile membrane by preventing direct contact but also enhance flow patterns and reduce mass transfer limitations, especially at low GHSV where these challenges are most significant. The easy integration of baffles has the potential to further amplify their potential. Overall POCS could lead to economic savings by both protecting the membrane and reducing mass transfer limitations (i.e. less membrane area required for a given separation). While this study focused on ammonia decomposition, the benefits demonstrated, namely improved transport properties, membrane protection, and design flexibility, are transferable to other membrane-assisted processes, particularly those constrained by heat and mass transfer, such as methane reforming or low-temperature Fischer-Tropsch synthesis.

CRediT authorship contribution statement

S. Richard: Writing – original draft, Investigation, Conceptualization. **D. Tasso:** Methodology, Investigation. **M. Rajana:** Writing – original draft, Investigation. **A. Saker:** Writing – review & editing, Supervision. **N. Meynet:** Supervision, Investigation. **B. Hary:** Writing – review & editing, Investigation. **S. Nardone:** Supervision, Resources. **G. Marino:** Writing – original draft, Investigation. **C. Italiano:** Writing – review & editing, Investigation. **A. Vita:** Writing – review & editing, Supervision. **F. Gallucci:** Writing – review & editing, Resources, Conceptualization.

Declaration of competing interest

The authors declare that they have no known competing financial

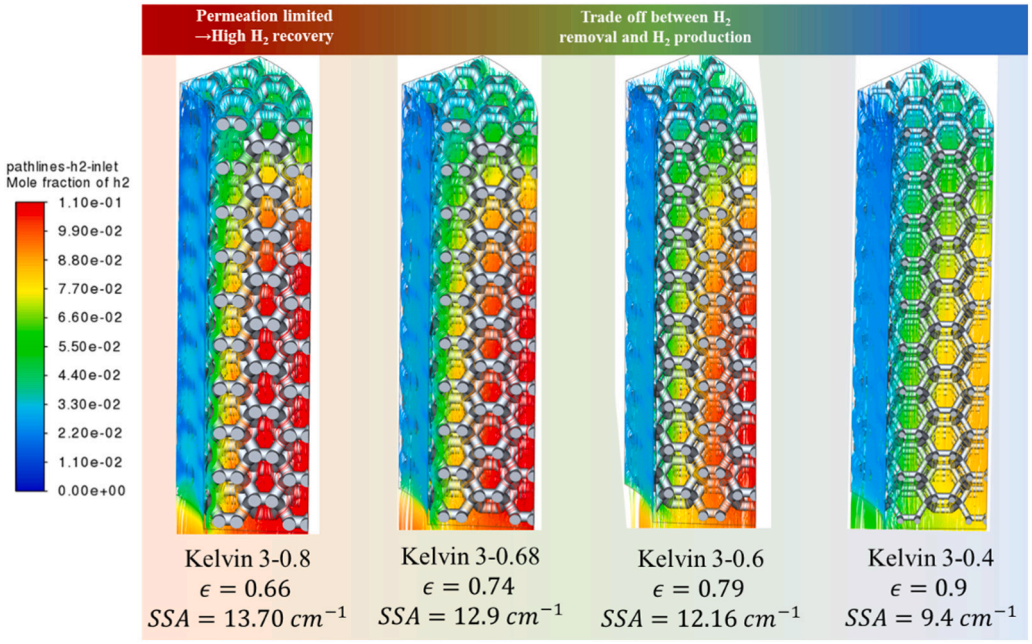

Fig. 11. Streamlines of the fluid velocity field analysis at different porosity (v_{in} = 0.01 m/s, GHSV = 4500 h^{-1}) on a representative portion of a membrane reactor.

interests or personal relationships that could have appeared to influence the work reported in this paper.

Appendix A. Supplementary data

Supplementary data to this article can be found online at https://doi.org/10.1016/j.cej.2025.166903.

Data availability

Data will be made available on request.

References

[1] M. Aziz, A.T. Wijayanta, A.B.D. Nandiyanto, Ammonia as effective hydrogen storage: a review on production, storage and utilization, Energies 13 (2020) 3062, https://doi.org/10.3390/en13123062.
[2] A. Valera-Medina, H. Xiao, M. Owen-Jones, W.I.F. David, P.J. Bowen, Ammonia for power, Prog. Energy Combust. Sci. 69 (2018) 63–102, https://doi.org/10.1016/j.pecs.2018.07.001.
[3] Y. Zhao, B.P. Setzler, J. Wang, J. Nash, T. Wang, B. Xu, Y. Yan, An efficient direct Ammonia fuel cell for affordable carbon-neutral transportation, Joule 3 (2019) 2472–2484, https://doi.org/10.1016/j.joule.2019.07.005.
[4] V. Dias, M. Pochet, F. Contino, H. Jeanmart, Energy and economic costs of chemical storage, Front. Mech. Eng. 6 (2020) 21, https://doi.org/10.3389/fmech.2020.00021.
[5] IEA, The Future of Hydrogen 203, 2019.
[6] M. Fecke, S. Garner, B. Cox, Review of Global Regulations for Anhydrous Ammonia Production, Use, and Storage, 2016.
[7] A. Yapicioglu, I. Dincer, A review on clean ammonia as a potential fuel for power generators, Renew. Sustain. Energy Rev. 103 (2019) 96–108, https://doi.org/10.1016/j.rser.2018.12.023.
[8] S. Richard, A. Ramirez Santos, F. Gallucci, PEM gensets using membrane reactors technologies: an economic comparison among different e-fuels, Int. J. Hydrogen Energy (2023) S0360319923032913, https://doi.org/10.1016/j.ijhydene.2023.06.312.
[9] K.E. Lamb, M.D. Dolan, D.F. Kennedy, Ammonia for hydrogen storage; a review of catalytic ammonia decomposition and hydrogen separation and purification, Int. J. Hydrogen Energy 44 (2019) 3580–3593, https://doi.org/10.1016/j.ijhydene.2018.12.024.
[10] I. Lucentini, X. Garcia, X. Vendrell, J. Llorca, Review of the decomposition of ammonia to generate hydrogen, Ind. Eng. Chem. Res. 60 (2021) 18560–18611, https://doi.org/10.1021/acs.iecr.1c00843.
[11] M. Asif, S. Sidra Bibi, S. Ahmed, M. Irshad, M. Shakir Hussain, H. Zeb, M. Kashif Khan, J. Kim, Recent advances in green hydrogen production, storage and commercial-scale use via catalytic ammonia cracking, Chem. Eng. J. 473 (2023) 145381, https://doi.org/10.1016/j.cej.2023.145381.
[12] C. Chen, K. Wu, H. Ren, C. Zhou, Y. Luo, L. Lin, C. Au, L. Jiang, Ru-based catalysts for ammonia decomposition: a mini-review, Energy Fuel 35 (2021) 11693–11706, https://doi.org/10.1021/acs.energyfuels.1c01261.
[13] V. Cechetto, L. Di Felice, F. Gallucci, Advances and perspectives of H $_2$ production from NH $_3$ decomposition in membrane reactors, Energy Fuel 37 (2023) 10775–10798, https://doi.org/10.1021/acs.energyfuels.3c00760.
[14] N. Itoh, Kinetic enhancement of ammonia decomposition as a chemical hydrogen carrier in palladium membrane reactor, Catal. Today 236 (Part A) (2014) 70–76, https://doi.org/10.1016/j.cattod.2014.02.054.
[15] J.P. Collins, J.D. Way, Catalytic decomposition of ammonia in a membrane reactor, J. Membr. Sci. 96 (1994) 259–274, https://doi.org/10.1016/0376-7388(94)00138-3.
[16] V. Cechetto, L. Di Felice, J.A. Medrano, C. Makhloufi, J. Zuniga, F. Gallucci, H2 production via ammonia decomposition in a catalytic membrane reactor, Fuel Process. Technol. 216 (2021) 106772, https://doi.org/10.1016/j.fuproc.2021.106772.
[17] J. Liu, X. Ju, C. Tang, L. Liu, H. Li, P. Chen, High performance stainless-steel supported Pd membranes with a finger-like and gap structure and its application in NH3 decomposition membrane reactor, Chem. Eng. J. 388 (2020) 124245, https://doi.org/10.1016/j.cej.2020.124245.
[18] Y. Park, J. Cha, H.-T. Oh, T. Lee, S.H. Lee, M.G. Park, H. Jeong, Y. Kim, H. Sohn, S. W. Nam, J. Han, C.W. Yoon, Y.S. Jo, A catalytic composite membrane reactor system for hydrogen production from ammonia using steam as a sweep gas, J. Membr. Sci. 614 (2020) 118483, https://doi.org/10.1016/j.memsci.2020.118483.
[19] S.H. Israni, B.K.R. Nair, M.P. Harold, Hydrogen generation and purification in a composite Pd hollow fiber membrane reactor: experiments and modeling, Catalysis Today 139 (2009) 299–311, https://doi.org/10.1016/j.cattod.2008.02.020.
[20] R. Sitar, J. Shah, Z. Zhang, H. Wikoff, J.D. Way, C.A. Wolden, Compact ammonia reforming at low temperature using catalytic membrane reactors, J. Membr. Sci. 644 (2022) 120147, https://doi.org/10.1016/j.memsci.2021.120147.
[21] J. Jiang, Q. Dong, K. McCullough, J. Lauterbach, S. Li, M. Yu, Novel hollow fiber membrane reactor for high purity H2 generation from thermal catalytic NH3 decomposition, J. Membr. Sci. 629 (2021) 119281, https://doi.org/10.1016/j.memsci.2021.119281.
[22] S. Richard, P. Olivier, M. Jegoux, C. Makhloufi, F. Gallucci, Membrane reactors technologies for e-fuel production & processing: a review, Int. J. Hydrogen Energy 112 (2025) 446–467, https://doi.org/10.1016/j.ijhydene.2025.01.361.
[23] H. Choi, S.H. Kim, J. Bae, S.P.R. Katikaneni, A. Jamal, A. Harale, S.N. Paglieri, J. H. Lee, CFD analysis and scale up of a baffled membrane reactor for hydrogen production by steam methane reforming, Comput. Chem. Eng. 165 (2022) 107912, https://doi.org/10.1016/j.compchemeng.2022.107912.
[24] A. Jandyal, I. Chaturvedi, I. Wazir, A. Raina, M.I. Ul Haq, 3D printing – a review of processes, materials and applications in industry 4.0, Sustainable Oper. Comput. 3 (2022) 33–42, https://doi.org/10.1016/J.SUSOC.2021.09.004.
[25] S. Danaci, Optimisation et integration de catalyseurs structurés pour la conversion de CO2 en methane, Université Grenoble Alpes, 2017.
[26] M. Klumpp, A. Inayat, J. Schwerdtfeger, C. Körner, R.F. Singer, H. Freund, W. Schwieger, Periodic open cellular structures with ideal cubic cell geometry: effect of porosity and cell orientation on pressure drop behavior, Chem. Eng. J. 242 (2014) 364–378, https://doi.org/10.1016/j.cej.2013.12.060.

[27] Z. Li, Y. Nie, B. Liu, Z. Kuai, M. Zhao, F. Liu, Mechanical properties of AlSi10Mg lattice structures fabricated by selective laser melting, Mater. Des. 192 (2020) 108709, https://doi.org/10.1016/j.matdes.2020.108709.

[28] C. Yan, L. Hao, A. Hussein, D. Raymont, Evaluations of cellular lattice structures manufactured using selective laser melting, Int. J. Mach. Tool Manuf. 62 (2012) 32–38, https://doi.org/10.1016/j.ijmachtools.2012.06.002.

[29] C. Busse, H. Freund, W. Schwieger, Periodic open cellular structures (POCS) as catalyst support for intensified heat transport in the partial oxidation of methanol to formaldehyde, Chem. Eng. J. 489 (2024) 151139, https://doi.org/10.1016/j.cej.2024.151139.

[30] R. Balzarotti, A. Bisaccia, M.C. Tripi, M. Ambrosetti, G. Groppi, E. Tronconi, Production and characterization of copper periodic open cellular structures made by 3D printing-replica technique, J. Adv. Manuf. Process. 2 (2020), https://doi.org/10.1002/amp2.10068.

[31] I. Kaur, P. Singh, Flow and thermal transport through unit cell topologies of cubic and octahedron families, International Journal of Heat and Mass Transfer 158 (2020) 119784, https://doi.org/10.1016/j.ijheatmasstransfer.2020.119784.

[32] C. Busse, H. Freund, W. Schwieger, Intensification of heat transfer in catalytic reactors by additively manufactured periodic open cellular structures (POCS), Chem. Eng. Process. Process Intensif. 124 (2018) 199–214, https://doi.org/10.1016/j.cep.2018.01.023.

[33] C. Ferroni, F.S. Franchi, M. Ambrosetti, M. Bracconi, G. Groppi, M. Maestri, E. Tronconi, Numerical and experimental investigation of pressure drop in periodic open cellular structures for intensification of catalytic processes, ACS Eng. Au (2022) acsengineeringau.1c00034, https://doi.org/10.1021/acsengineeringau.1c00034.

[34] Z. Cheng, R. Xu, P.-X. Jiang, Morphology, flow and heat transfer in triply periodic minimal surface based porous structures, International Journal of Heat and Mass Transfer 170 (2021) 120902, https://doi.org/10.1016/j.ijheatmasstransfer.2021.120902.

[35] F.M. Baena-Moreno, M. González-Castaño, J.C. Navarro de Miguel, K.U.M. Miah, R. Ossenbrink, J.A. Odriozola, H. Arellano-García, Stepping toward efficient microreactors for CO $_2$ Methanation: 3D-printed Gyroid geometry, ACS Sustain. Chem. Eng. 9 (2021) 8198–8206, https://doi.org/10.1021/acssuschemeng.1c01980.

[36] A. Montebelli, C.G. Visconti, G. Groppi, E. Tronconi, C. Ferreira, S. Kohler, Enabling small-scale methanol synthesis reactors through the adoption of highly conductive structured catalysts, Catalysis Today 215 (2013) 176–185, https://doi.org/10.1016/j.cattod.2013.02.020.

[37] D. Merino, O. Sanz, M. Montes, Effect of the thermal conductivity and catalyst layer thickness on the Fischer-Tropsch synthesis selectivity using structured catalysts, Chem. Eng. J. 327 (2017) 1033–1042, https://doi.org/10.1016/j.cej.2017.07.003.

[38] C. Italiano, M.A. Ashraf, L. Pino, C.W.M. Quintero, S. Specchia, A. Vita, Rh/CeO2 thin catalytic layer deposition on alumina foams: catalytic performance and controlling regimes in biogas reforming processes, Catalysts 8 (2018) 448, https://doi.org/10.3390/catal8100448.

[39] J.J. Bolívar Caballero, T. Han, R. Svanberg, I.N. Zaini, H. Yang, R. Gond, P. Cao, T. Lewin, P.G. Jönsson, W. Yang, Advanced application of a geometry-enhanced 3D-printed catalytic reformer for syngas production, Energy Convers. Manag. 287 (2023) 117071, https://doi.org/10.1016/j.enconman.2023.117071.

[40] C. Li, S. Yuan, X. Yao, X. Yu, B. Li, S.-T. Tu, Structured nanoporous copper catalysts prepared by laser powder bed fusion and dealloying for on-board methanol steam reforming, Fuel 347 (2023) 128367, https://doi.org/10.1016/j.fuel.2023.128367.

[41] I. Lucentini, G. García Colli, C. Luzi, I. Serrano, L. Soler, N.J. Divins, O.M. Martínez, J. Llorca, Modelling and simulation of catalytic ammonia decomposition over Ni-Ru deposited on 3D-printed CeO2, Chem. Eng. J. 427 (2022) 131756, https://doi.org/10.1016/j.cej.2021.131756.

[42] R. Balzarotti, M. Ambrosetti, M. Arnesano, A. Anglani, G. Groppi, E. Tronconi, Periodic open cellular structures (POCS) as enhanced catalyst supports: optimization of the coating procedure and analysis of mass transport, Appl. Catal. Environ. 283 (2021) 119651, https://doi.org/10.1016/j.apcatb.2020.119651.

[43] Q. Wei, H. Li, G. Liu, Y. He, Y. Wang, Y.E. Tan, D. Wang, X. Peng, G. Yang, N. Tsubaki, Metal 3D printing technology for functional integration of catalytic system, Nat. Commun. 11 (2020) 4098, https://doi.org/10.1038/s41467-020-17941-8.

[44] P.H. Ho, M. Ambrosetti, G. Groppi, E. Tronconi, R. Palkovits, G. Fornasari, A. Vaccari, P. Benito, Structured catalysts-based on open-cell metallic foams for energy and environmental applications, in: Studies in Surface Science and Catalysis, Elsevier, 2019, pp. 303–327, https://doi.org/10.1016/B978-0-444-64127-4.00015-X.

[45] T. Knorr, P. Heinl, J. Schwerdtfeger, C. Körner, R.F. Singer, B.J.M. Etzold, Process specific catalyst supports—selective electron beam melted cellular metal structures coated with microporous carbon, Chem. Eng. J. 181 (2012) 725–733, https://doi.org/10.1016/j.cej.2011.10.009.

[46] A. Vita, C. Italiano, C. Fabiano, L. Pino, M. Laganà, V. Recupero, Hydrogen-rich gas production by steam reforming of n-dodecane, Appl. Catal. Environ. 199 (2016) 350–360, https://doi.org/10.1016/j.apcatb.2016.06.042.

[47] R. Balzarotti, C. Cristiani, L.F. Francis, Spin coating deposition on complex geometry substrates: influence of operative parameters, Surf. Coat. Technol. 330 (2017) 1–9, https://doi.org/10.1016/j.surfcoat.2017.09.077.

[48] R. Balzarotti, A. Beretta, G. Groppi, E. Tronconi, A comparison between washcoated and packed copper foams for the intensification of methane steam reforming, react. Chem. Eng. 4 (2019) 1387–1392, https://doi.org/10.1039/C9RE00125E.

[49] R.J.W. Voncken, I. Roghair, M. van Sint Annaland, A numerical study on concentration polarization in 3D cylindrical fluidized beds with vertically immersed membranes, Chem. Eng. Sci. 205 (2019) 299–318, https://doi.org/10.1016/j.ces.2019.05.010.

[50] R. Ma, B. Castro-Dominguez, A.G. Dixon, Y.H. Ma, Scalability of multitube membrane modules for hydrogen separation: technical considerations, issues and solutions, J. Membr. Sci. 564 (2018) 887–896, https://doi.org/10.1016/j.memsci.2018.08.003.

[51] A. Caravella, L. Melone, Y. Sun, A. Brunetti, E. Drioli, G. Barbieri, Concentration polarization distribution along Pd-based membrane reactors: a modelling approach applied to water-gas shift, Int. J. Hydrogen Energy 41 (2016) 2660–2670, https://doi.org/10.1016/j.ijhydene.2015.12.141.

[52] F. Lucci, A. Della Torre, G. Montenegro, R. Kaufmann, P. Dimopoulos Eggenschwiler, Comparison of geometrical, momentum and mass transfer characteristics of real foams to kelvin cell lattices for catalyst applications, Int. J. Heat Mass Transf. 108 (2017) 341–350, https://doi.org/10.1016/j.ijheatmasstransfer.2016.11.073.

[53] S. Richard, D. Tasso, M. Rajana, A. Saker, A. Ramirez Santos, C. Makhloufi, N. Meynet, B. Hary, S. Nardone, G. Marino, M. Thomas, C. Italiano, A. Vita, F. Gallucci, Comparison of thermo-hydraulic performance among different 3D printed periodic open cellular structures, Chem. Eng. J. 492 (2024) 152005, https://doi.org/10.1016/j.cej.2024.152005.

[54] V. Papetti, P. Dimopoulos Eggenschwiler, A. Della Torre, F. Lucci, A. Ortona, G. Montenegro, Additive manufactured open cell polyhedral structures as substrates for automotive catalysts, International Journal of Heat and Mass Transfer 126 (2018) 1035–1047, https://doi.org/10.1016/j.ijheatmasstransfer.2018.06.061.

[55] M. Bracconi, M. Ambrosetti, M. Maestri, G. Groppi, E. Tronconi, Analysis of the effective thermal conductivity of isotropic and anisotropic periodic open cellular structures for the intensification of catalytic processes, Chem. Eng. Process. Process Intensif. 158 (2020) 108169, https://doi.org/10.1016/j.cep.2020.108169.

[56] C. Ferroni, M. Bracconi, M. Ambrosetti, M. Maestri, G. Groppi, E. Tronconi, A fundamental investigation of gas/solid heat and mass transfer in structured catalysts based on periodic open cellular structures (POCS), Ind. Eng. Chem. Res. 60 (2021) 10522–10538, https://doi.org/10.1021/acs.iecr.1c00215.

[57] H. Doh, H.Y. Kim, G.H. Kim, Influence of cation substitutions based on ABO3 perovskite materials, Sr1−xYxTi1−yRuyO3−δ, on ammonia dehydrogenation, ACS Sustain. Chem. Eng. (2017) 9370–9379.

[58] S. Soisuwan, J. Panpranot, D.L. Trimm, P. Praserthdam, A study of alumina–zirconia mixed oxides prepared by the modified Pechini method as co catalyst supports in CO hydrogenation, Appl. Catal. Gen. 303 (2006) 268–272, https://doi.org/10.1016/j.apcata.2006.02.011.

[59] E. Fernandez, A. Helmi, K. Coenen, J. Melendez, J.L. Viviente, D.A. Pacheco Tanaka, M. van Sint Annaland, F. Gallucci, Development of thin Pd–ag supported membranes for fluidized bed membrane reactors including WGS related gases, Int. J. Hydrogen Energy 40 (2015) 3506–3519, https://doi.org/10.1016/j.ijhydene.2014.08.074.

[60] N. de Nooijer, F. Gallucci, E. Pellizzari, J. Melendez, D.A. Pacheco Tanaka, G. Manzolini, M. van Sint Annaland, On concentration polarisation in a fluidized bed membrane reactor for biogas steam reforming: modelling and experimental validation, Chem. Eng. J. 348 (2018) 232–243, https://doi.org/10.1016/j.cej.2018.04.205.

[61] A. Di Carlo, L. Vecchione, Z. Del Prete, Ammonia decomposition over commercial Ru/Al2O3 catalyst: an experimental evaluation at different operative pressures and temperatures, Int. J. Hydrogen Energy 39 (2014) 808–814, https://doi.org/10.1016/j.ijhydene.2013.10.110.

[62] S. Chiuta, R.C. Everson, R.C. Everson, H.W.J.P. Neomagus, H.W.J.P. Neomagus, D. G. Bessarabov, Ammonia decomposition for decentralized hydrogen production in microchannel reactors: Experiments and CFD simulations, in: M. Sankir, N. D. Sankir (Eds.), Hydrogen Production Technologies, John Wiley & Sons, Inc., Hoboken, NJ, USA, 2017, pp. 77–111, https://doi.org/10.1002/9781119283676.ch2.

[63] W.-H. Chen, W.-S. Chou, R.-Y. Chein, A.T. Hoang, J.C. Juan, Multiple-objective optimization on ammonia decomposition using membrane reactor, Int. J. Hydrogen Energy (2023) S0360319923023339, https://doi.org/10.1016/j.ijhydene.2023.05.081.

[64] J.L. Cerrillo, N. Morlanés, S.R. Kulkarni, N. Realpe, A. Ramírez, S.P. Katikaneni, S. N. Paglieri, K. Lee, A. Harale, B. Solami, A. Jamal, S. Mani Sarathy, P. Castaño, J. Gascon, High purity, self-sustained, pressurized hydrogen production from ammonia in a catalytic membrane reactor, Chem. Eng. J. (2021) 134310, https://doi.org/10.1016/j.cej.2021.134310.